

# Label-free, all-optical detection, imaging and tracking of a single protein

J. Ortega Arroyo,<sup>†</sup> J. Andrecka,<sup>†</sup> K. M. Spillane,<sup>†,¶</sup> N. Billington,<sup>‡</sup> Y. Takagi,<sup>‡</sup> J. R. Sellers,<sup>‡</sup> and P. Kukura<sup>\*,†</sup>

*Physical and Theoretical Chemistry Laboratory, South Parks Road, Oxford OX1 3QZ, UK,  
and Laboratory of Molecular Physiology, National Heart, Lung and Blood Institute,  
National Institutes of Health, Bethesda, Maryland 20892, USA*

E-mail: philipp.kukura@chem.ox.ac.uk

KEYWORDS: single molecule detection, label-free, bio-sensing, myosin 5a, interferometric scattering microscopy

## Abstract

Optical detection of individual proteins requires fluorescent labeling. Cavity and plasmonic methodologies enhance single molecule signatures in the absence of any labels, but have struggled to demonstrate routine and quantitative single protein detection. Here, we used interferometric scattering microscopy not only to detect, but also to image and nanometrically track the motion of single myosin 5a heavy meromyosin molecules without the use of labels or any nanoscopic amplification. Together with the simple experimental arrangement, an intrinsic independence from strong electronic

---

<sup>\*</sup>To whom correspondence should be addressed

<sup>†</sup>Physical and Theoretical Chemistry Laboratory, South Parks Road, Oxford OX1 3QZ, UK

<sup>‡</sup>Laboratory of Molecular Physiology, National Heart, Lung and Blood Institute, National Institutes of Health, Bethesda, Maryland 20892, USA

<sup>¶</sup>Current address: MRC National Institute for Medical Research, The Ridgeway Mill Hill, London, NW7 1AA, UK

transition dipoles and a detection limit of  $<60$  kDa, our approach paves the way toward non-resonant, label-free sensing and imaging of nanoscopic objects down to the single protein level.

Single molecule optics has contributed considerably to our understanding of a broad range of fundamental processes in physics, chemistry and biology. Following the first optical detection of single molecules by absorption,<sup>1</sup> all subsequent methodologies relied on the observation of fluorescence emission to differentiate the species of interest from an otherwise overwhelming background.<sup>2</sup> Despite its many advantages, fluorescence labeling has a number of drawbacks such as limited observation periods due to photobleaching and blinking<sup>3</sup> and artifacts induced by the orientation of the transition dipoles.<sup>4</sup> Most importantly, chemical or genetic labeling is necessary to visualize single molecules since most biological species are non-fluorescent.

As a consequence, many attempts have been made to find all-optical single molecule alternatives to fluorescence detection. Surface enhanced Raman spectroscopy exhibits remarkable sensitivity and even chemical specificity,<sup>5</sup> but requires nanometer-precise positioning of the analyte close to atomically rough and difficult to control metallic structures. Approaches based on extinction,<sup>6</sup> stimulated emission,<sup>7</sup> and photothermal<sup>8</sup> detection have recently demonstrated single molecule sensitivity even for non-fluorescent molecules. All these techniques, however, require sophisticated noise or background suppression methodologies and strong electronic transition dipoles at the optical detection wavelength, a property that most biological molecules fundamentally lack.

Achieving non-resonant detection at the single protein level has thus been thought to require amplification of the weak optical signature from a single molecule. Cavity and plasmonic sensors have reported single molecule sensitivity in this fashion,<sup>9-11</sup> but require complex experimental setups and are subject to large variations in the single molecule signals, making quantitative studies difficult. [In addition, imaging and studying dynamics on the nanoscale, are unachievable by design because it is difficult to obtain spatial information since](#)

movement of the analyte does not result in a spatially distinct signal. Here, we show that interferometric scattering microscopy (iSCAT)<sup>12–14</sup> can detect, image and track the motion of individual proteins without the need for any labels in biologically compatible conditions, demonstrated here with the molecular motor, myosin 5a heavy meromyosin (HMM).

Interferometric scattering microscopy relies on the detection of scattered light from the sample in an optical microscope.<sup>12,13</sup> Imaging is performed in a reflective geometry, similar to well established approaches such as interference reflection microscopy<sup>15,16</sup> or reflection interference contrast microscopy,<sup>17</sup> but with higher sensitivity achieved through the use of coherent light sources and optimized detection methodologies.<sup>18</sup> The area illuminated through the imaging objective consists of a sparse sample of weak scatterers placed at the focus, which allows most of the incident light to pass through the sample (Figure 1A). The glass/water interface reflects ~0.5 % of the incident light, which is collected by the objective together with a fraction of the light scattered by the nano-objects in the sample.

The corresponding experimental setup is similar to a standard confocal scanning microscope with the exception that the reflected and scattered photons are extracted efficiently by combining a quarter wave plate with a polarizing beamsplitter rather than being rejected by a fluorescence filter (Figure 1B). In addition, the collected light is not passed through a pinhole but is instead imaged onto a CMOS camera. Rapid scanning of the incident beam by acousto-optical deflectors at a rate much faster than the exposure time of the camera achieves uniform illumination of the sample. Using a loosely focused beam in this illumination scheme significantly reduces interference fringes caused by multiple reflections inside the objective compared to standard wide-field illumination.<sup>13</sup> The final image produced in this fashion consists of small features on top of a large background.

The high sensitivity of iSCAT makes it possible to visualize very weak scatterers without the use of any labels. As an example, individual actin filaments bound to a microscope cover glass are readily observed (Figure 1C). In addition to the filaments, the nanometer roughness of the cover glass generates a static background that appears as noise, but is reproducible

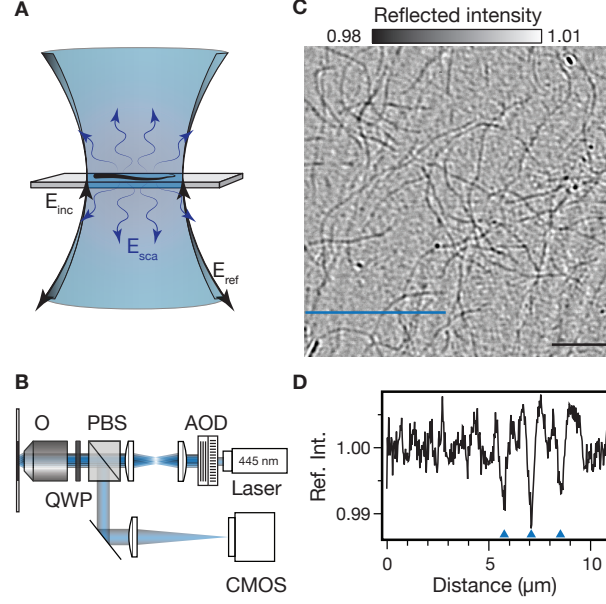


Figure 1: Interferometric scattering microscopy of biomolecules. (A) Schematic of the sample region including incident  $E_{inc}$ , reflected  $E_{ref}$  and scattered  $E_{sca}$  light fields. (B) Experimental setup. O: objective, QWP: quarter wave plate, PBS: polarizing beamsplitter, AOD: acousto-optic deflector. (C) iSCAT image of individual, unlabeled actin filaments adhered to a microscope cover glass. Pixel non-uniformity and inhomogeneity is removed by flat-fielding using a temporal median filter (See Methods). Scale bar:  $5\ \mu\text{m}$  (black line). (D) Indicated cut from (C) corresponding to  $11.5\ \mu\text{m}$  (blue line). The blue arrowheads indicate the three actin filaments visible along the indicated cut in (C).

in consecutive acquisitions. The indicated cross section in Figure 1D illustrates the relative magnitudes of the filaments and surface roughness signals. While filaments generate a signal on the order of 1.0 %, the background fluctuations of 0.3 % ensure that the filaments remain faintly visible above the background. The magnitude of the observed iSCAT signal for individual actin filaments can be understood by considering its linear dependence on the polarizability and thus molecular weight of the scatterer. Within a diffraction limited spot ( $200\ \text{nm}$ ) containing a portion of an actin filament, there are about 75 actin subunits of total molecular mass  $3.1\ \text{MDa}$ . A SV40 virus-like particle with a molecular mass of  $15\ \text{MDa}$  produces an iSCAT contrast of 4.5 % in our current experimental arrangement,<sup>13</sup> resulting in an expected actin iSCAT contrast of 0.9 %, in excellent agreement with our experimental observations (Figure 1D).



The linear dependence of the scattering signal on the number of protein molecules in the focus of the microscope poses the question whether individual proteins can be detected label-free with iSCAT. We chose a recombinant heavy meromyosin (HMM)-like fragment of the motor myosin 5a as a test case since it has been very well characterized as a processive actin-dependent motor using a combination of different single molecule techniques and its processive properties are a robust indicator of single molecules.<sup>19</sup> We introduced GFP at the C-terminus of myosin 5a HMM to enable direct comparison with established single molecule fluorescence-based imaging without having to use separate preparations, but emphasize that the small size (40 kDa) and the weak transition dipole at 445 nm of GFP are insufficient to generate an iSCAT signal of  $>0.01\%$ . Based on the above calculation and the molecular weight of myosin 5a HMM (502 kDa) the iSCAT contrast for a single myosin 5a HMM molecule is expected to be on the order of  $0.15\%$ . Such signals are smaller than those generated both by individual actin filaments and the roughness of the glass making it difficult to observe them directly in images such as that shown in Figure 1C. However, upon addition of ATP myosin 5a HMM moves along actin filaments while all other features of the iSCAT image remain stationary. Therefore, subtraction of an image containing all stationary iSCAT features from the original frames, which we term differential imaging, will reveal changes in sample scattering due to mobile scatterers, in this case myosin 5a.

Under ideal conditions, the only noise source that could overwhelm the signal originating from weak scatterers for differential imaging are fluctuations in the background level caused by shot noise in the detection of photoelectrons by the imaging system. Commercially available digital cameras usually saturate at  $10^4 - 10^5$  photoelectrons per pixel resulting in a baseline noise on the order of  $0.3\%$  root-mean-squared (RMS) in the best case for individual images.

Given that the background is constant, we can generate a low-noise image of the static iSCAT background consisting largely of actin filaments and the glass substrate by replacing each pixel with the median value from a sequence of images or averaging together several

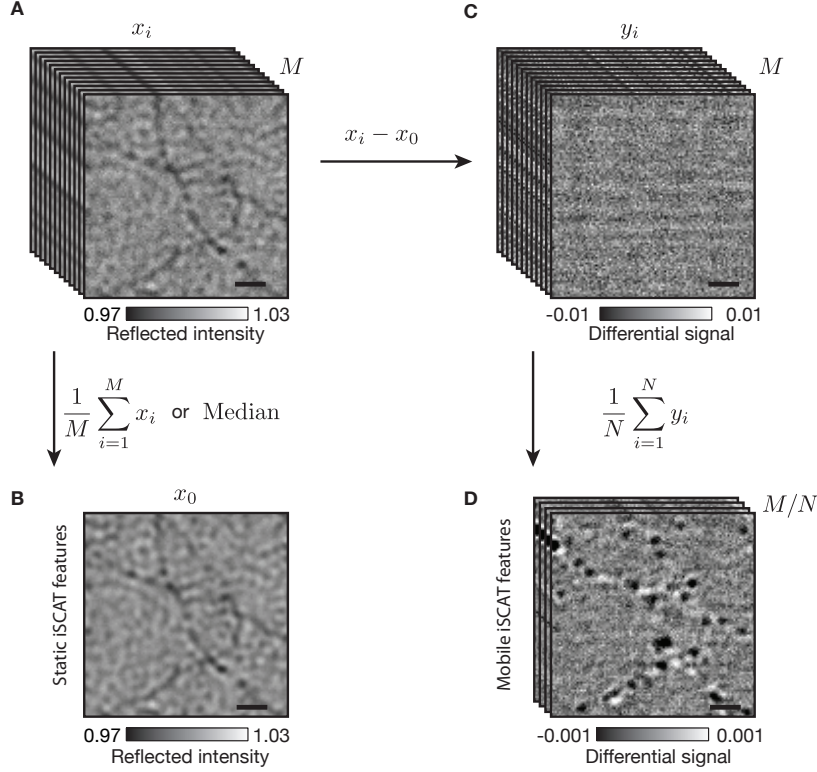


Figure 2: Interferometric scattering detection of myosin 5a HMM at the single molecule level. (A) Sequence containing  $M$  iSCAT images,  $x_i$ , of actin filaments on a microscope cover glass in the presence of myosin 5a HMM. Camera exposure time set at 0.40 ms with a frame time of 0.58 ms,  $[\text{ATP}] = 5 \mu\text{M}$ . (B) An image containing purely stationary iSCAT features obtained by taking the median or averaging over the sequence of images in (A). (C) Sequence of  $M$  differential iSCAT images,  $y_i$ , obtained by subtracting the stationary iSCAT features from the image sequence in (A). (D) Time averaged differential images generated by binning  $N = 170$  consecutive frames together. Note the order of magnitude decrease in  $z$ -scale from (C) to (D). Scale bars:  $1 \mu\text{m}$  (black line).

frames (Figure 2B). After subtraction of the median from each individual image, the differential images show signals due to mobile iSCAT features and shot noise (Figure 2C), which can be reduced further by summing consecutive images and thus accumulating more photoelectrons. We remark that the median background image does not need to be acquired either in the absence of myosin 5a or ATP as computing the median intrinsically removes any non-stationary contributions that occur either as a consequence of binding/unbinding of myosin 5a or movement in the presence of ATP. In some cases, we used temporal averaging to further improve our signal to noise ratios, for example for nanometric tracking,

although such an approach was only necessary due to sample drift that was not controllable in the current experimental setup (See Methods section). Our camera allowed detection of an  $104 \times 104$  pixel<sup>2</sup> area at a frame rate of 1.7 kHz. Time averaging consecutive differential frames to a bandwidth of 10 Hz increases the electron count per pixel to  $2 \times 10^7$ , and thus reduces the baseline fluctuations to 0.024 %. Upon time averaging the differential images, we observed several diffraction-limited spots that coincide spatially with the actin filaments in the presence of ATP (Figure 2D and Supporting Movie S1). The specific binding to actin together with the processive motion along these filaments, suggests that these features are due to myosin 5a HMM molecules. Importantly, myosin molecules become visible above the background because they are the only mobile component of the sample and are thus not removed by the subtraction of the median image generated from the image stack.

The dramatic effect of time averaging on the visibility of small iSCAT signals is illustrated by plotting image cross sections as a function of averaged images (Figure 3A). For individual image subtraction, the standard deviation amounts to 0.3 % as expected from the well depth of the imaging camera. As the number of images averaged increases, however, the shot noise drops to the point where an iSCAT signal of the order of 0.2 % becomes clearly visible. The evolution of the standard deviation of the background as a function of the number of averaged images shows shot noise induced behavior down to the 60 kDa level (Figure 3B). At this point, the achievable behavior begins to deviate from shot noise due to the introduction of other noise sources that affect the differential images, in our case mechanical drift ( $< 10$  nm) of the sample position and small fluctuations in laser intensity.

Although specific binding and motion along actin filaments strongly suggest the observation of individual myosin 5a HMM molecules, further proof requires comparison with established fluorescence<sup>20</sup> or optical tweezer<sup>21</sup> based single-molecule assays. We therefore performed nanometric tracking of individual myosin 5a HMM molecules. The distributions of stepping kinetics (Figure 4A), run lengths at saturating ATP concentrations (1 mM) (Figure 4B) and the velocity dependence on ATP concentration (Figure 4C) all show excellent

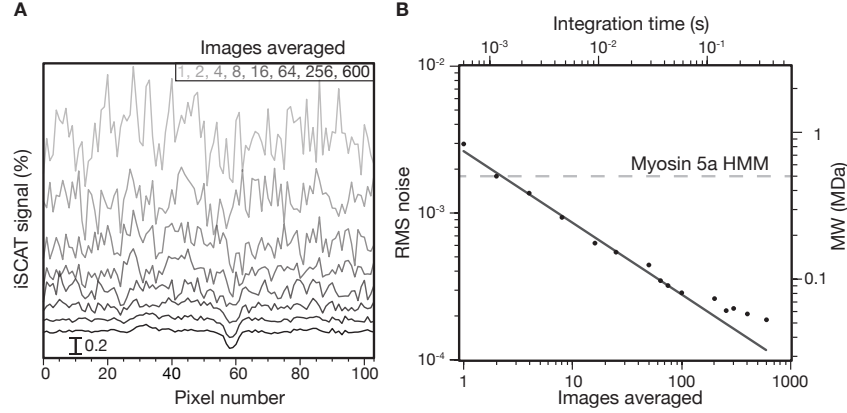


Figure 3: iSCAT as an all-optical single protein sensor. (A) One dimensional cut across a single differential myosin 5a HMM iSCAT signal for integration times ranging from 0.58 to 348.00 ms. The signal in (A) is assigned to be a single myosin 5a HMM molecule due to its processive nature, characteristic 37 nm steps and contrast value of 0.18%. The cross section was chosen along the x-axis with no particular orientation relative to the underlying actin filament whose iSCAT signal is removed by the differential imaging scheme. (B) Background noise as a function of the number of images averaged. Solid line indicates shot noise behavior. We added a second vertical axis corresponding to the molecular weight detectable at a signal to noise ratio of 1 as a function of integration time. In the case of myosin 5a this number corresponds to 1 ms. The dashed grey line represents the molecular weight of myosin 5a HMM. The theoretical detection limit thus corresponds to 60 kDa at an integration time of 300 ms in the current experimental arrangement.

agreement with previous single molecule studies.<sup>20–23</sup> In addition, we evaluated the iSCAT contrast for 249 different molecules from several tens of image stacks analyzed as shown in Figure 2. We obtained a single distribution with an iSCAT contrast centered around 0.18 % in good agreement with our theoretical prediction of the iSCAT contrast for a single myosin 5a molecule (0.15 %). The spread of contrasts is likely due to small variations in focusing, the lack of control over the orientation of the protein relative to the incident polarization and possible displacements of the protein relative to the substrate. For scatterers with a contrast of 0.3 %, the localization accuracy was on the order of 5 nm and thus sufficient to observe distinct, 37 nm steps as expected for myosin 5a (Figure 4E).

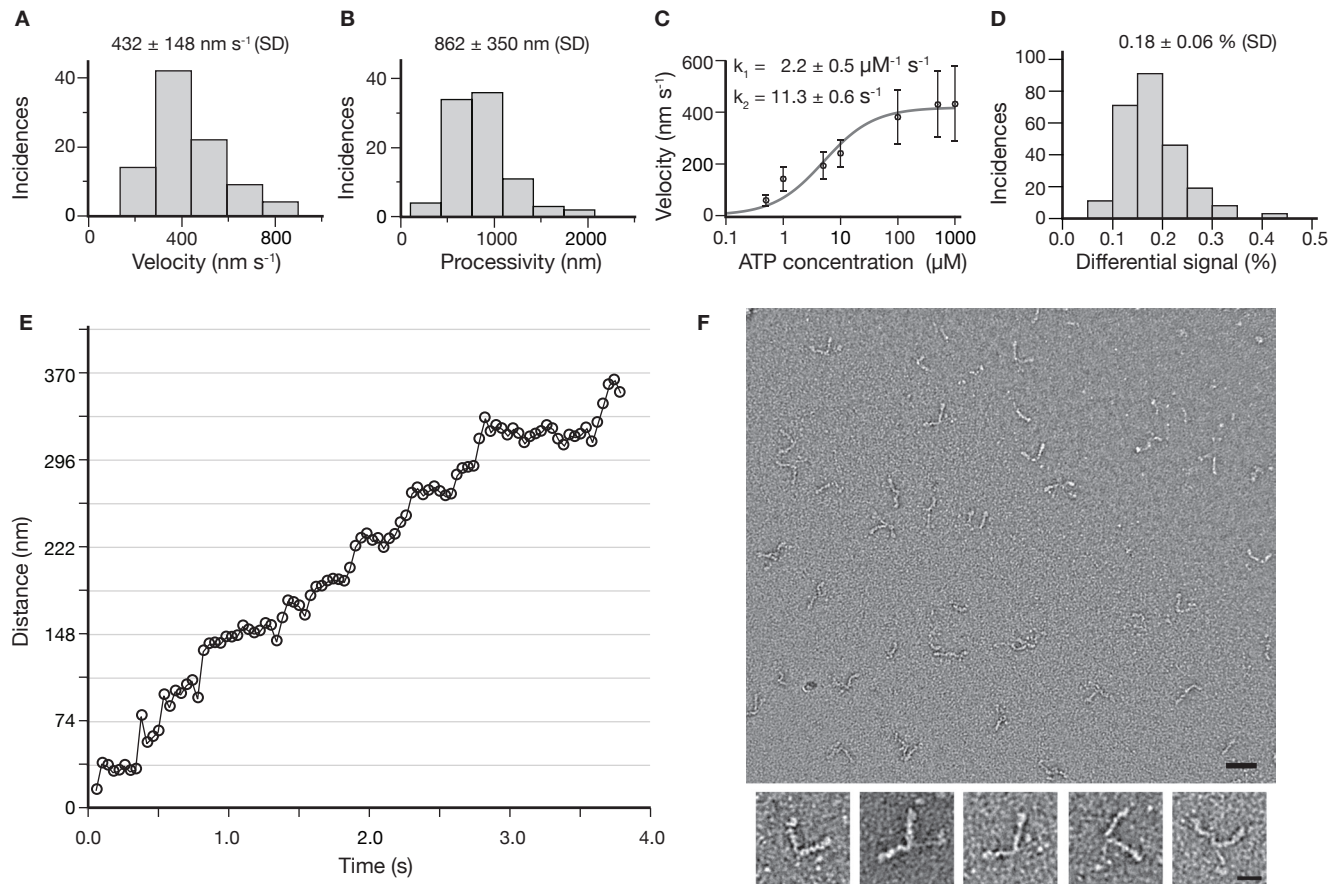


Figure 4: Myosin 5a HMM processivity characterized by iSCAT at the single molecule level. (A, B) Run velocity and processivity at saturating ATP concentrations (1 mM,  $n = 91$ ). (C) Run velocity as a function of ATP concentration. The solid curve represents the best fit of the run velocity data to the relationship  $V = ds / (1/k_1[ATP] + 1/k_2)$ , where  $ds$  represents the average step size assumed to be 37 nm,  $k_1$  the second order ATP binding rate constant and  $k_2$  the first order ADP release rate constant. (D) Histogram of iSCAT contrasts obtained from finding the center of mass of 249 separate processive molecules. All visible processive signatures from 15 recordings were included in the histogram and no additional pre-selection was performed **170 frames originally recorded at 1.7 kHz were averaged for this analysis**. (E) Distance traveled for a single myosin 5a molecule with contrast of 0.31 % at 10  $\mu$ M ATP concentration. **Imaging speed: 1 kHz averaged to 25 Hz (see Supporting Movie S4)**. (F) Sample quality assessment of myosin 5a HMM used in this study by electron microscopy. Upper panel shows an electron micrograph of the construct, scale bar: 50 nm. Lower panels show examples of individual myosin 5a HMM molecules at higher magnification, scale bar: 20 nm. The sample was confirmed to be without aggregates and dimeric, with bound light chains.

The above observations and the excellent match between expected and observed iSCAT contrast for a single myosin 5a HMM molecule together with the following arguments strongly

suggest that the observed moving objects are single myosin 5a molecules and not aggregates or other species. The same preparation of myosin 5a HMM investigated by negative staining electron microscopy under similar concentrations and ionic strengths as used in the single molecule motility experiments showed a very homogeneous distribution of objects consisting predominantly of double-headed myosin molecules with a coiled-coil tail and with no larger aggregates that could lead to exaggerated iSCAT signal (Figure 4F).<sup>24</sup> The movement of objects was very robust, which is inconsistent with aggregates given the negligible amount of aggregation observed in the preparation (Movie S1). If the moving objects represented only a few percent of the total myosin 5a present, then the actin filament would have to be saturated with moving, non-detectable single myosin 5a molecules. These conclusions are further supported by single molecule fluorescence assays performed with the same preparation of myosin 5a HMM by detecting the fluorescence of the GFP fusion moiety. We observed very similar amounts of both bound and transiently binding molecules in iSCAT and fluorescence measurements performed on the same sample consecutively on different instruments (Supporting Movies S2, S3). Simultaneous iSCAT and fluorescence, although in principle possible,<sup>13</sup> was difficult to achieve here due to the rapid photobleaching of GFP by the iSCAT illumination beam at 445 nm.

Label-free detection does not allow for the observation of signatures such as photoblinking, bleaching or anti-bunching of the emission that act as proof for the observation of single molecules. We thus chose myosin Va HMM because its processive properties have become generally accepted as a signature for the presence of single molecules through a variety of optical experiments.<sup>20-23</sup> In addition, the observation of specific binding to actin (Supporting Movies S1, S2) mimics the operation of any sensor, i.e. the comparison of a signal in the presence and absence of the analyte. In cavity-based techniques<sup>9</sup> the signal is the resonance frequency, while for plasmonic sensors it is the maximum of the plasmon resonance.<sup>10,11</sup> In iSCAT it is the surface scattering in the absence or presence of a single protein.

iSCAT has three important advantages over all currently available approaches to label-

free single molecule sensing. Firstly, single molecule signals show a single distribution about a maximum signal that is directly proportional to the mass of the analyte (Fig. 4D). This is in stark contrast to current optical technologies capable of detecting single molecules without labels, such as plasmonic and cavity-based sensors whose signals fluctuate between zero and a maximum signal, making quantification much more difficult. Secondly, iSCAT provides spatial information that is useful in combination with patterned surfaces often used in sensing applications and enables direct comparison of affinities in a single measurement. Finally, the experimental setup is comparatively trivial, requiring only an inverted microscope and a glass coverslip as the sensor.

Our results disprove the notion that the scattering cross sections of single proteins are orders of magnitude too small to be detected in an optical microscope. Even complex spectroscopic investigations now routinely operate with sensitivities at the  $10^{-5}$  level or below,<sup>25</sup> at which detection and imaging of small proteins on the order of 60 kDa would still occur at excellent SNRs of 10 with iSCAT. Critically, however, the presented detection modality does not require any specific molecular properties, such as strong transition dipoles, nor does it depend on sophisticated methodologies to reduce laser intensity noise or nanoscopic amplification of the weak single molecule signal. Instead, the imaging camera performs noise reduction automatically through the accumulation of detected photoelectrons with time and no ultrastable laser sources or specific refractive index environments are necessary. Together with the possibility of combining iSCAT with single molecule fluorescence<sup>13</sup> and the potential for unlimited observation times due to a lack of photobleaching our results enable novel applications from bio-sensing to multidimensional tracking of single biomolecules.

## Acknowledgments

P.K. is supported by the John Fell Fund, a career acceleration fellowship by the EPSRC (EP/H003541) and an ERC starting grant (NanoScope). K.S. was supported by a fellowship from the National Institute of Biomedical Imaging and Bioengineering, National Institutes of

Health (FEB013960). J.O.A was supported by a scholarship from CONACyT to pursue his doctoral work (scholar: 213546). J.A. was supported by a Marie Curie Fellowship (330215). J.R.S. was supported by the intramural funds from the National Heart, Lung and Blood Institute, National Institutes of Health (ZIA HL004229). The authors thank the Electron Microscopy Core Facility of the NHLBI for support and the use of facilities.

## MATERIALS AND METHODS

### Experimental setup

The experimental setup is similar to that described in Ref. 13. Briefly, the output of a 445 nm diode laser is spatially filtered and adjusted to 2 mm beam diameter before passing through two acousto-optic deflectors (AOD, Gooch and Housego). The beam deflections generated by the AODs are imaged with telecentric lenses into the back focal plane of an oil immersion objective (Olympus PLAPON 1.42 NA, 60x) after passing through a polarizing beam splitter (PBS). The small beam diameter underfills the back aperture of the objective to generate a focal spot of  $\sim 1 \mu\text{m}$  full width at half maximum (FWHM). A quarter wave plate before the objective causes any reflected and scattered light by the sample to get reflected by the PBS before being imaged onto a CMOS (Photonfocus MV-D1024-160-CL-8) camera at either 167x or 333x magnification by choosing the appropriate focal length imaging lens. The incident power is adjusted to achieve near-saturation of the CMOS camera amounting to 2.5 and 10  $\text{kW}/\text{cm}^2$  at the sample at 1.0 ms exposure time for the two magnifications.

The two AOD channels are scanned in a sawtooth fashion by separate, phase locked function generators at 84 and 83 kHz, respectively. Both the absolute and relative frequencies are chosen to induce the smallest detectable fluctuations in the background light intensity on the timescale of the camera exposure time. Even though the frequency difference (1 kHz) nominally suggests a minimum exposure time of 1 ms, this requirement is relaxed by the large spot size. For a FWHM of  $1 \mu\text{m}$  few tens of scans over an area of  $10 \times 10 \mu\text{m}^2$  are



sufficient to generate a highly uniform illumination. At the given scan speeds, this process only takes  $\sim 100 \mu\text{s}$ , much faster than the shortest exposure time. Any spot broadening induced by the limited speed of the acoustic wave in the deflector only serves to further smoothen the illumination. Rapid scanning and illumination of an area four times larger than what is imaged by the camera avoids the introduction of diffraction fringes from the edges of the sawtooth pattern and eventually achieves shot noise limited sensitivity toward the  $10^{-4}$  level.

## Data recording and analysis

To produce images such as Figure 1C it is necessary to remove any constant background caused by residual reflections and illumination inhomogeneities. To do so we record 100 images while manually moving the sample stage and then replace each pixel by the temporal median value of the frame sequence to generate an optimal flat field image that is independent of the sample. After division by the flat field image we obtain sample-specific images with shot noise limited sensitivity, which simplifies the initial alignment and choosing an appropriate region. Finding the correct focal point is critical and can be estimated by maximizing the contrast from individual actin filaments, although fine adjustment during the recording is necessary. The latter is achieved by recording a single image and subtracting it from the live preview that only reveals changes in the sample scattering compared to the original background image. In the presence of myosin 5a HMM, such a subtraction leads to the differential images such as those shown in Movie S3. [To reduce the effects of sample drift at least along the optical axis, we stabilize the focus by monitoring the back-reflection of a totally internal reflected beam at 633 nm.](#)

To generate an image containing all the static iSCAT features we first determined the number of frames in the acquired sequence that lacked a myosin 5a HMM signal. This was achieved by subtracting the last frame from all other frames in the sequence and then time averaging 20 of these differential frames together to reveal potential myosin 5a HMM signals.

If the number of frames lacking a myosin HMM signal exceeded 100 then these images were averaged to produce the static iSCAT background image. Otherwise a temporal median filter was performed over the range of images in which the myosin 5a HMM molecule was processive, typically greater than 1000 frames, to avoid ghosting artefacts. Contrast values for single myosin 5a HMM were determined by the pixel value corresponding to the centre of mass of the point spread function.

For myosin 5a detection, we initially used 166X magnification, 104 x 104 pixel<sup>2</sup> field of view at 63.6 nm/pixel, a frame rate of 1.7 kHz and time averaged the differential images to 10 Hz. For tracking, we increased the magnification to 333x with a 128 x 128 pixel<sup>2</sup> field of view and a frame rate of 1.0 kHz to improve the electron count and therefore the signal to noise ratio. Nanometric tracking was performed by time averaging the differential images to 25 Hz and then fitting the point spread function to a two dimensional Gaussian.

## **Interferometric scattering microscopy sample preparation**

Rabbit skeletal muscle actin<sup>26</sup> and mouse myosin 5a HMM<sup>27</sup> with a C-terminal GFP were prepared as described and stored in liquid nitrogen until used. A 20  $\mu$ M actin stock solution was prepared in polymerization buffer (10 mM imidazole, 50 mM KCl, 1 mM MgCl<sub>2</sub>, 1 mM EGTA, pH 7.3 containing 1.7 mM DTT, 3 mM ATP). Actin was diluted in motility buffer (MB; 20 nM MOPS pH 7.3, 5 mM MgCl<sub>2</sub>, 0.1 mM EGTA) 50-100 times.

Borosilicate glass cover glasses (No. 1.5, 24 x 50 mm, VWR) were cleaned by sequential rinsing with Milli-Q water, ethanol and water. They were then dried under a stream of dry nitrogen and exposed to UV/ozone for 8 minutes at 50 W power using a plasma cleaner (Diener Electronic, Plasma System Femto). All cover glass was used within one day of cleaning. A single flow cell was then assembled using double-sided transparent tape (Scotch) and a second cover glass (No. 1, 24 x 40 mm, VWR).

The flow cell was rinsed with 1 mg/mL solution of poly(ethylene glycol)-poly-l-lysine (PEG-PLL) branch copolymer (Surface Solutions SuSoS, Switzerland) in PBS and incubated

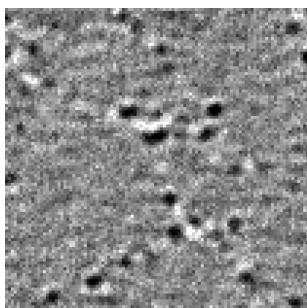
for 30 min. Next, it was washed twice with MB and actin solution was added. After 5 minutes of incubation the chamber was washed with MB and the surface was blocked by adding 1 mg/ml BSA in MB buffer and subsequent incubation for 5 minutes. 2-10 nM myosin solution (MB containing 40 mM KCl, 5 mM DTT, 0.1 mg/ml BSA and 5  $\mu$ M calmodulin) was added, incubated for 5 minutes and then washed. Upon addition of ATP, myosin movement was observed.

## Electron microscope sample preparation

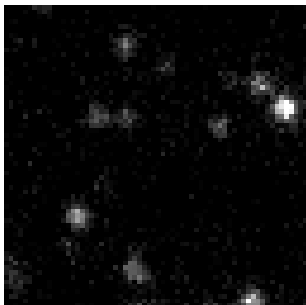
Myosin 5a HMM was diluted to 50 nM in buffer containing 10 mM MOPS (pH 7.0), 2mM  $MgCl_2$ , 0.1 mM EGTA, and 40 mM KCl. A 5- $\mu$ l drop of sample was applied to a carbon-coated copper grid (pretreated with UV light) and stained with 1 % uranyl acetate. Micrographs were recorded at 60,000X on a JEOL 1200EX II microscope. Data were recorded on an AMT XR-60 CCD camera. Catalase crystals were used as a size calibration standard.

## Supporting Information Available

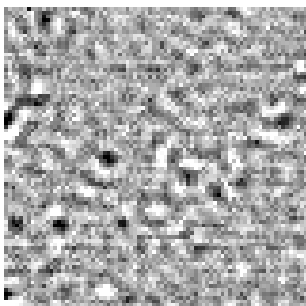
Supporting movies S1-S4.



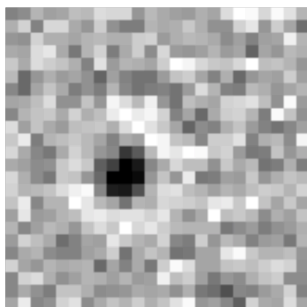
Movie S1: iSCAT Imaging the processive motion of individual myosin 5a HMM molecules along actin filaments. Raw data was recorded at 1.7 kHz with 167X magnification (64 nm/pixel), background subtracted via temporal median filtering and then time averaged down to 10 Hz to produce the displayed movie. The movie frame rate is set to 25 Hz and the field of view corresponds to 6.6  $\mu$ m  $\times$  6.6  $\mu$ m.



Movie S2: Total internal reflection fluorescence imaging of single processive myosin 5a HMM molecules. Each myosin contains two GFP moieties that give rise to the fluorescence signal upon excitation at 473 nm. Frames were recorded with 100 ms exposure time under frame transfer mode at a frame rate of 10 Hz with 333X magnification (72 nm/pixel) by an iXon3 860 EM-CCD camera. The movie is played at 10 Hz and the field of view corresponds to  $4.6 \mu\text{m} \times 4.6 \mu\text{m}$ .



Movie S3: Consecutive imaging of the same myosin 5a HMM sample as in Movie S2 by interferometric scattering microscopy. Raw data was recorded at 1.0 kHz with 333X magnification (32 nm/pixel), background subtracted via temporal median filtering, spatially binned to 64 nm/pixel, and then time averaged to 10 Hz to produce the displayed movie. The movie is played at 10 Hz and the field of view corresponds to  $5.08 \mu\text{m} \times 5.08 \mu\text{m}$ . [The length of the recording was limited by the storage capacity of the computer used for data acquisition.](#)



Movie S4: Nanometric tracking of a single myosin 5a HMM molecule recorded by interferometric scattering microscopy. Raw data was recorded at 1.0 kHz with 333X magnification (32 nm/pixel), background subtracted via temporal median filtering, spatially binned to 64 nm/pixel, and then time averaged to 25 Hz to produce the displayed movie. Movie is played at 25 Hz and the field of view corresponds to  $1.53 \times 1.53 \mu\text{m}^2$ . The displayed movie has been up-scaled six-fold for ease of visualization with no further modification of the data.

This material is available free of charge via the Internet at <http://pubs.acs.org/>.

## References

- (1) Moerner, W. E.; Kador, L. *Physical Review Letters* **1989**, *62*, 2535–2538.
- (2) Orrit, M.; Bernard, J. *Physical Review Letters* **1990**, *65*, 2716–2719.
- (3) Dickson, R. M.; Cubitt, A. B.; Tsien, R. Y.; Moerner, W. E. *Nature* **1997**, *388*, 355–358.
- (4) Enderlein, J.; Toprak, E.; Selvin, P. R. *Optics express* **2006**, *14*, 8111–8120.
- (5) Nie, S.; Emory, S. R. *Science* **1997**, *275*, 1102–1106.
- (6) Kukura, P.; Celebrano, M.; Renn, A.; Sandoghdar, V. *The Journal of Physical Chemistry Letters* **2010**, *1*, 3323–3327.
- (7) Chong, S.; Min, W.; Xie, X. S. *The Journal of Physical Chemistry Letters* **2010**, *1*, 3316–3322.
- (8) Gaiduk, A.; Yorulmaz, M.; Ruijgrok, P. V.; Orrit, M. *Science* **2010**, *330*, 353–356.

- (9) Armani, A. M.; Kulkarni, R. P.; Fraser, S. E.; Flagan, R. C.; Vahala, K. J. *Science* **2007**, *317*, 783–787.
- (10) Ament, I.; Prasad, J.; Henkel, A.; Schmachtel, S.; Sönnichsen, C. *Nano Letters* **2012**, *12*, 1092–1095.
- (11) Zijlstra, P.; Paulo, P. M. R.; Orrit, M. *Nature Nanotechnology* **2012**, *7*, 379–382.
- (12) Lindfors, K.; Kalkbrenner, T.; Stoller, P.; Sandoghdar, V. *Physical Review Letters* **2004**, *93*, 037401.
- (13) Kukura, P.; Ewers, H.; Müller, C.; Renn, A.; Helenius, A.; Sandoghdar, V. *Nature Methods* **2009**, *6*, 923–927.
- (14) Ortega Arroyo, J.; Kukura, P. *Physical Chemistry Chemical Physics* **2012**, *14*, 15625.
- (15) Vašíček, A. *Optics and Spectroscopy* **1961**, *11*, 128.
- (16) Curtis, A. *The Journal of Cell Biology* **1964**, *20*, 199–215.
- (17) Zilker, A.; Engelhardt, H.; Sackmann, E. *Journal de Physique* **1987**, *48*, 2139–2151.
- (18) Celebrano, M.; Kukura, P.; Renn, A.; Sandoghdar, V. *Nature Photonics* **2011**, *5*, 95–98.
- (19) Sellers, J. R.; Veigel, C. *Current Opinion in Cell Biology* **2006**, *18*, 68–73.
- (20) Yildiz, A.; Forkey, J. N.; McKinney, S. A.; Ha, T.; Goldman, Y. E.; Selvin, P. R. *Science* **2003**, *300*, 2061–2065.
- (21) Rief, M.; Rock, R. S.; Mehta, A. D.; Mooseker, M. S.; Cheney, R. E.; Spudich, J. A. *Proceedings of the National Academy of Sciences* **2000**, *97*, 9482–9486.
- (22) Snyder, G. E.; Sakamoto, T.; Hammer, J. A., III; Sellers, J. R.; Selvin, P. R. *Biophysical Journal* **2004**, *87*, 1776–1783.

- (23) Baker, J. E.; Krementsova, E. B.; Kennedy, G. G.; Armstrong, A.; Trybus, K. M.; Warshaw, D. M. *Proceedings of the National Academy of Sciences* **2004**, *101*, 5542–5546.
- (24) Walker, M. L.; Burgess, S. A.; Sellers, J. R.; Wang, F.; Hammer, J. A.; Trinick, J.; Knight, P. J. *Nature* **2000**, *405*, 804–807.
- (25) Dobryakov, A. L.; Kovalenko, S. A.; Weigel, A.; Pérez-Lustres, J. L.; Lange, J.; Müller, A.; Ernsting, N. P. *Review of Scientific Instruments* **2010**, *81*, 113106.
- (26) Spudich, J. A.; Watt, S. *Journal of Biological Chemistry* **1971**, *246*, 4866–4871.
- (27) Wang, F.; Chen, L.; Arcucci, O.; Harvey, E. V.; Bowers, B.; Xu, Y.; Hammer, J. A.; Sellers, J. R. *Journal of Biological Chemistry* **2000**, *275*, 4329–4335.

# Graphical TOC Entry

